



MID-AMERICA TRANSPORTATION CENTER

Report # MATC-MS&T: 133-3

Final Report

WBS: 25-1121-0005-133-3

UNIVERSITY OF
Nebraska
Lincoln

THE UNIVERSITY
OF IOWA

THE UNIVERSITY OF
KU
KANSAS

MISSOURI
S&T

LINCOLN
UNIVERSITY
MISSOURI



UNIVERSITY OF
Nebraska
Omaha

University of Nebraska
Medical Center

KU MEDICAL
CENTER
The University of Kansas

Performance of Corroded Piles Subjected to Eccentric Loads Before and After Repair - Phase III

Mohamed ElGawady, PhD

Benavides Professor

Department of Civil, Architectural, and
Environmental Engineering

Missouri University of Science and Technology

MISSOURI
S&T

2024

A Cooperative Research Project sponsored by
U.S. Department of Transportation- Office of the Assistant
Secretary for Research and Technology

The contents of this report reflect the views of the authors, who are responsible for the facts and the accuracy of the information presented herein. This document is disseminated in the interest of information exchange. The report is funded, partially or entirely, by a grant from the U.S. Department of Transportation's University Transportation Centers Program. However, the U.S. Government assumes no liability for the contents or use thereof.

MATC

Performance of Corroded Piles Subjected to Eccentric Loads Before and After Repair – Phase III

Mohamed ElGawady, Ph.D.
Benavides Professor
Civil, Architectural and Environmental
Engineering (CArEE)
Missouri University S&T

A Report on Research Sponsored by

Mid-America Transportation Center
University of Nebraska–Lincoln

September 2024

Technical Report Documentation Page

1. Report No. 25-1121-005-133-3	2. Government Accession No.	3. Recipient's Catalog No.	
4. Title and Subtitle Performance of Corroded Piles Subjected to Eccentric Loads Before and After Repair		5. Report Date September 2024	
		6. Performing Organization Code	
7. Author(s) Mohamed ElGawady, 0000-0001-6928-9875		8. Performing Organization Report No. This is also where the WBS # appears	
9. Performing Organization Name and Address Mid-America Transportation Center Prem S. Paul Research Center at Whittier School 2200 Vine St. Lincoln, NE 68583-0851		10. Work Unit No. (TRAIS)	
		11. Contract or Grant No. 69A3551747107	
12. Sponsoring Agency Name and Address Office of the Assistant Secretary for Research and Technology 1200 New Jersey Ave., SE Washington, D.C. 20590		13. Type of Report and Period Covered Final Report January 2020 – December 2021	
		14. Sponsoring Agency Code MATC TRB RiP No. 91994-55	
15. Supplementary Notes			
16. Abstract H-Piles are a well-known method used to support bridges because they have a small cross-section relative to their capacity. Steel H-piles have various levels of corrosion caused by environmental conditions; therefore, there is an urgent need to determine the residual axial capacity of corroded H-piles. Most design manuals allow some tolerance for eccentricities during pile-loading, which might cause a significant drop in corrosion. This report presents the results of four full-scale H-piles tested with two eccentric loads of 10% and 30%. Corrosion was simulated using mechanical reduction in the thickness, cuts in the flanges, and webs of the piles. The axial strengths of the piles were calculated using the design procedures of the American Institute of Steel Construction (AISC). This report describes experimental and numerical pushout testing of the previously corroded H-piles embedded into concrete-filled FRP jackets. Different repair techniques and types of different FRP jackets, confinement ratios, and head stud stiffnesses were investigated. The report results revealed that eccentricity reduced the capacity of the corroded piles, especially for piles with severe corrosion in the form of cuts and voids in the flanges and web, respectively. Moreover, the repair method using CFRP jackets with mounted head studs significantly increased the axial strength capacity of the repaired corroded piles.			
17. Key Words Steel H-piles, Axial Capacity, Eccentric loads, CFRP, Corrosion, LS-DYNA		18. Distribution Statement	
19. Security Classif. (of this report) Unclassified	20. Security Classif. (of this page) Unclassified	21. No. of Pages 40	22. Price

Table of Contents

Disclaimer	vii
Abstract	viii
Executive Summary	ix
Chapter 1 Piles Preparation and Milling	1
1.1 Test Specimens	1
1.1.1 Material Properties	3
1.1.2 Test Setup and Loading Protocol	4
1.1.3 Instrumentation	6
Chapter 2 Piles repair design and installation	10
2.1 CFRP Jacket	11
2.1.1 Headed Studs	11
2.1.2 Longitudinal Reinforcing Bars	11
2.2 Concrete	13
2.3 Fabrication and Installation of the Repair System	14
2.3.1 Preparation of the Steel Pile	14
2.3.2 Preparation of the CFRP Jackets	15
2.3.3 Preparation of the Steel Cage	16
2.3.4 Installing the Repair Jacket and Filling with SCC	16
2.3.5 Instrumentation	17
Chapter 3 Piles Testing	20
3.1 Results and Discussion	20
Chapter 4 Finite element modeling of the repaired piles	25
4.1 FE Modeling	25
4.1.1 Model Geometry	25
4.1.2 Material Models	25
4.1.3 Boundary Conditions and Loading	29
4.1.4 Model Results	30
Chapter 5 Summary And Conclusions	36
References	38

List of Figures

Figure 1.1 Representative column for eccentricity	2
Figure 1.2 Schematic of milling configuration	3
Figure 1.3 Steel H-piles average stress-strain curve (a) flange, and (b) web.	5
Figure 1.4 Test setup: (a) drawing, and (b) picture.....	7
Figure 1.5 Loading instruments: (a) hydraulic jack, and (b) rail track with rolling cylinders.....	7
Figure 1.6 Swivel plates (a) maximum rotation, and (b) installed in the setup.	8
Figure 1.7 Eccentricity of the swivel with the pile.	8
Figure 1.8 Distribution of the strain gages on H-piles: (a) Type 1, and (b) Type 2.	9
Figure 2.1 All threaded bars and heavy-duty nuts used as HSs.....	12
Figure 2.2 Distributions of the HSs in the three H-piles: (a) R-1, (b) R-2, and (3) R-3.	12
Figure 2.3 Longitudinal reinforcement in the repair region: (a) closed bar profile, (b) distributions of rebars, and (c) reinforcement cage.....	13
Figure 2.4 ASTM tests: (a) Slump flow, (b) Passing ability using J-ring, and (c) L-box.	14
Figure 2.5 (a) Magnetic drill used to drill holes for the HSs, and (b) general distribution for studs	15
Figure 2.6 Specimens after CFRP Installation.....	17
Figure 2.7 Strain gauges distribution on the flanges and web of H-pile.....	17
Figure 2.8 Strain gauges distribution on the CFRP cross-section (a) Cross section (b) longitudinal direction	18
Figure 2.9 String potentiometer vertical and horizontal measurements	19
Figure 3.1 Failure during the experimental W00-F00, and (b) W70V-F50C	21
Figure 3.2 Axial force vs Axial shortening relation: (a) W00-F00 (Ref.), (b) W70V-F50C, (c) W70V-F50C-10%, (d) W70V-F50C-30%.....	22
Figure 3.3 Experimental axial load vs. displacement curves (a) R1, (b) R2, and (c) R3	23
Figure 4.1 FE of the repaired piles and HSs layout of (a) R1, (b) R2, and (c) R3.	27
Figure 4.2 FE modeling: (a) 3D view of the repaired steel pile, (b) steel H-pile, (c) CFRP tube, (d) concrete filling, and (e) steel rebar.....	28
Figure 4.3 Axial load vs. displacement curves (a) R1, (b) R2, and (c) R3.....	31
Figure 4.4 Failure modes of the simulated repaired pile R1 (a) exp., (b) FE whole system, (c) Exp. steel pile localized buckling, (d) FE steel pile localized buckling, and (e) concrete encasement stress concentration	32
Figure 4.5 Stress concentration at the tips of flanges on the concrete encasement.	33
Figure 4.6 Failure modes of the simulated repaired pile R2 (a) exp., (b and c) FE.....	34
Figure 4.7 Failure modes of the simulated repaired pile R3 (a and c) exp., (b and d) FE.....	35

List of Tables

Table 1.1 Test Matrix for H-Piles	3
Table 1.2 Actual Dimensions of the Tested Piles	4
Table 1.3 Sectional Properties at Minimum Cross Section based on the Measured Dimensions ..	5
Table 1.4 Mechanical Properties of Steel H-Pile Flange and Web.....	6
Table 2.1 Mixture Used for the Concrete	14
Table 2.2 Arrangement of HSs in Different Test Specimens	16
Table 3.1 Results for the Tested Piles.....	21
Table 4.1 Mechanical Properties of the Steel Rebar Elements	29

List of Abbreviations (optional)

Mid-America Transportation Center (MATC)

Nebraska Transportation Center (NTC)

Disclaimer

The contents of this report reflect the views of the authors, who are responsible for the facts and the accuracy of the information presented herein. This document is disseminated in the interest of information exchange. The report is funded, partially or entirely, by a grant from the U.S. Department of Transportation's University Transportation Centers Program. However, the U.S. Government assumes no liability for the contents or use thereof.

Abstract

H-Piles are a well-known method used to support bridges because they have a small cross-section relative to their capacity. Steel H-piles have various levels of corrosion caused by environmental conditions; therefore, there is an urgent need to determine the residual axial capacity of corroded H-piles. Most design manuals allow some tolerance for eccentricities during pile-loading, which might cause a significant drop in corrosion. This report presents the results of four full-scale H-piles tested with two eccentric loads of 10% and 30%. Corrosion was simulated using mechanical reduction in the thickness, cuts in the flanges, and webs of the piles. The axial strengths of the piles were calculated using the design procedures of the American Institute of Steel Construction (AISC). This report describes experimental and numerical pushout testing of the previously corroded H-piles embedded into concrete-filled FRP jackets. Different repair techniques and types of different FRP jackets, confinement ratios, and head stud stiffnesses were investigated. The report results revealed that eccentricity reduced the capacity of the corroded piles, especially for piles with severe corrosion in the form of cuts and voids in the flanges and web, respectively. Moreover, the repair method using CFRP jackets with mounted head studs significantly increased the axial strength capacity of the repaired corroded piles.

Executive Summary

This report summarizes the details of experimental work and finite element modeling conducted to evaluate: 1) the remaining axial capacity of steel H-piles having severe corrosion, and 2) the performance of repaired corroded steel H-piles. The research consisted of five large steel H-piles (10×42) milled to represent the lost cross-sectional area associated with corrosion and tested under concentric and eccentric axial loads.

This report includes five chapters. Chapter 1 presents preparation of the corroded piles. Corrosion will be simulated through a reduction in the targeted cross section using a Bridgeport milling machine. Chapter 2 covers pile repair design and installation using CFRP jackets and head studs. Chapter 3 illustrates an experimental work to assess the load-carrying capacity of corroded piles subjected to concentric and eccentric axial loads. Chapter 4 presents the results of analytical and experimental work on H-piles repaired using FRP jackets. Chapter 5 summarizes the main conclusions and findings of the research project.

The report findings revealed that eccentricity reduced the capacity of the corroded piles, especially for the piles with severe corrosion in the form of cuts and voids in the flanges and web, respectively. Moreover, the repair method using CFRP jackets with mounted head studs significantly increased the axial strength capacity of the repaired corroded piles.

Chapter 1 Piles Preparation and Milling

An extensive literature review of corroded H-piles was carried out in previous research by the PI [1-18]. Therefore, this project will start by testing a reference specimen and three corroded piles. It is worth noting that no reference pile was tested under eccentric load during Phase I of this project [17]. This chapter will focus on preparing the corroded piles. Corrosion will be simulated through a reduction in the targeted cross section using a Bridgeport milling machine. Reduction of a section will be carried out from both sides of the targeted web and/or flanges to maintain a symmetric section. The corroded sections will have different severity and hence different reductions in the corroded sections. Reductions up to 50% and 70% will be carried out in the flanges and webs, respectively.

1.1 Test Specimens

Four full-scale H-piles with a cross-section of 250 x 85 mm (10 x 42 in.), and a length of 3050 mm (120 in.) were investigated during this research. The piles consisted of four groups: 1) un-corroded reference, 2) minorly corroded, 3) moderately corroded, and 4) severely corroded. Each group had two percentages of eccentricity measured from the center of the pile: 10% and 30% (Table 1.1 and Fig. 1.1). The performance of the piles under eccentric loads was also compared to that of similar piles tested under concentric loads available in the literature [17-19]. The minor and moderate corrosion was simulated by reducing the thickness of the web by 70% and/or flanges by 50% from the original thicknesses, while the severe corrosion had both reductions in the web and flange thickness with the addition of 152.4 x 95.25 mm (6 x 3.75 in.) void in the web and two 152.4 mm (6 in.) diameter semi-circle cuts in each flange (Fig. 1.2). The percentages of reduction in the thickness and cuts were selected to mimic real corrosion scenarios while investigating wide spectrum of corroded sections. All corrosion was simulated

by reducing the thickness over a 304.8 mm (12 in.) section located in the middle of each pile. The measured geometric properties of the smallest cross-section of the tested specimens are presented in Tables 1.2 and 1.3.

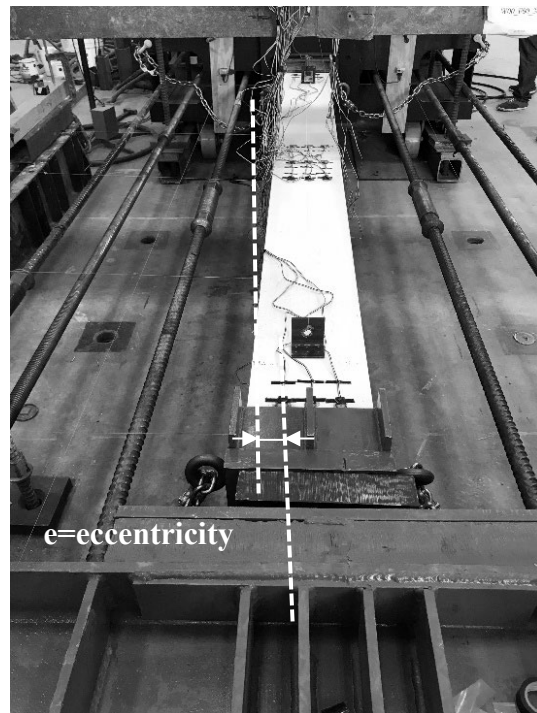


Figure 1.1 Representative column for eccentricity

Each pile specimen is assigned a three-segment identifier to describe the web, flange, and eccentricity. For example, the identifier W70V-F50C-30% would describe a web (W) with a 70% reduction in thickness and a void (V) in the first segment, a flange (F) with a 50% reduction in thickness and a cut (C) in the second segment, and a 30% eccentricity in the loading.

Table 1.1 Test Matrix for H-Piles

Eccentricity %	H-Pile #	Web		Flange		Corrosion Extension (Lc)
		Reduction %	Void	Reduction %	Cut	
0%	W00-F00[17,18]	--	--	--	--	--
0%	W70V-F50C [17,18]	70	V	50	C	304.8mm (12in.)
10%	W70V-F50C-10%	70	V	50	C	304.8mm (12in.)
30%	W70V-F50C-30%	70	V	50	C	304.8mm (12in.)

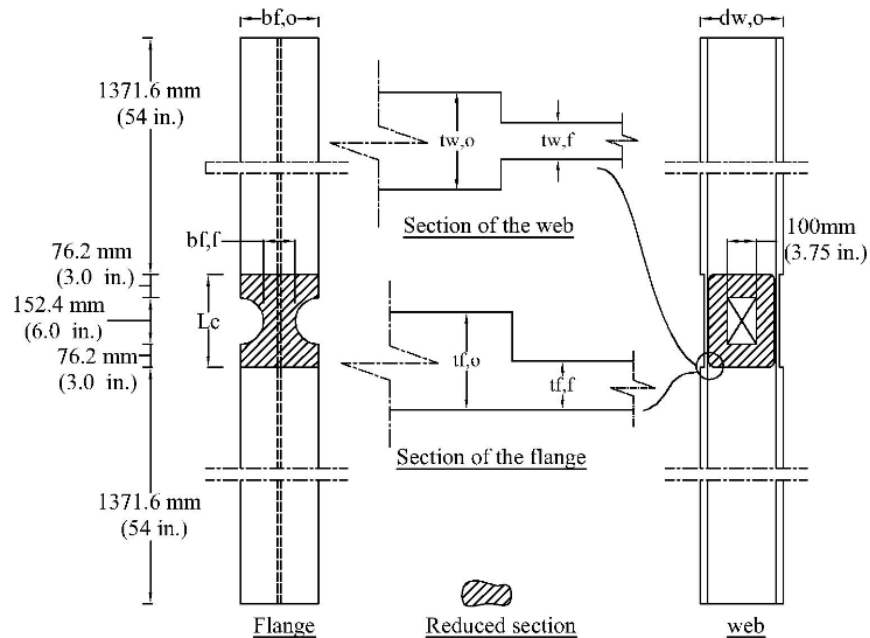


Figure 1.2 Schematic of milling configuration

1.1.1 Material Properties

Three replicate steel coupons were cut from a flange and a web of a pile and tested per the ASTM E8/E8M [22] to determine their tensile strengths (Table 1.4). The axial strains were measured using a 25.4 mm (1-in.) extensometer attached to the mid-height of each coupon (Fig.

1.3). The steel coupons displayed distinct yielding stress followed by yielding plateau and strain hardening until the coupons reached their ultimate strengths (Table 1.4).

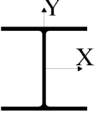
Table 1.2 Actual Dimensions of the Tested Piles

Groups	H-Pile #	Original Section			Corroded Section				
		Flange		Web	Reduced Flange			Reduced Web	
		$t_{f,o,N}$ (in.)	$t_{f,o,S}$ (in.)	$t_{w,o}$ (in.)	$t_{f,f,N}$ (in.)	$t_{f,f,S}$ (in.)	$b_{f,f}$ (in.)	$t_{w,f}$ (in.)	Void (in.)
Reference	W00-F00 [17,18]	0.425	0.426	0.374	--	--	--	--	--
Severe corrosion	W70V-F50C [17,18]	0.419	0.426	0.368	0.21	0.213	4.073	0.12	6x3.75
	W70V-F50C-10%	0.422	0.425	0.375	0.211	0.213	4.075	0.113	6x3.75
	W70V-F50C-30%	0.426	0.423	0.373	0.213	0.211	4.071	0.112	6x3.75

1.1.2 Test Setup and Loading Protocol

Specimens were tested using a 4450 kN (1000 kips) self-reacting frame which has three main components, two fixed beams, and a movable beam between the two fixed ones. All beams were connected by six post-tensioning bars, each having a diameter of 35 mm (1.375 in.) (Fig. 1.4 – 1.7). The moving beam had one degree of freedom and its unidirectional movement was controlled through two guided rails and four wheels.

Table 1.3 Sectional Properties at Minimum Cross Section based on the Measured Dimensions

Designation	Shape	A_{min} (in. ²)	A_f (in. ²)	A_w (in. ²)	A_w/A_f	r_{min} (in.)	L (in.)	KL/r_{min}	$b_f/2t_f$	h/t_w
W00-F00		12.00	8.56	3.00	0.35	2.46	120	48.80	11.85	21.46
W70V-F50C		2.48	1.73	0.11	0.07	0.98	120	122.68	9.61	8.96
W70V-F50C-10%		2.45	1.73	0.12	0.07	0.97	120	123.78	9.61	8.23
W70V-F50C-30%		2.45	1.74	0.13	0.07	3.75	120	31.99	9.57	8.10

Note: kl/r_{min} was determined using r_{min} at the reduced section
 Units conversion: 1 in.=25.4 mm

Each specimen had pin-pin boundary conditions. Each end of a specimen was placed inside a steel box, which was attached to a semi-sphere at the required eccentricity (Fig. 1.4). The semi-sphere was allowed to move on a swivel plate which in turn was connected to either the moving beam at one end of the pile or the fixed beam at the other end. The load was applied against the moving beam using two 2225 kN (500 kips) hydraulic cylinders and an oil pump with an average rate of 155 kN/min (35 kips/min) until failure occurred.

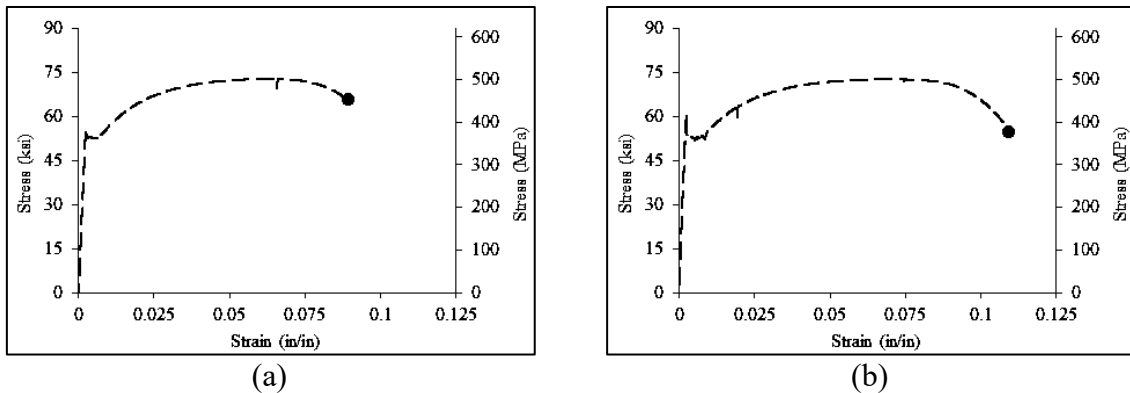


Figure 1.3 Steel H-piles average stress-strain curve (a) flange, and (b) web.

Table 1.4 Mechanical Properties of Steel H-Pile Flange and Web

Section	Yield stress MPa (ksi)	Ultimate stress MPa (ksi)	Modulus of Elasticity (E) GPa (10³ ksi)
Flange	324 (47)	517 (75)	181 (26.25)
Web	407 (59)	503 (73)	182 (26.40)

1.1.3 Instrumentation

Six 890 kN (200 kips) load cells were placed on post-tensioning bars to record the applied force on each bar, which represented the total force applied to a test specimen. To measure the loads in the bars, each bar also had a strain gauge that was monitored during the test. Furthermore, to monitor the behavior of each specimen, forty-nine strain gauges were attached to seven sections over the length of the specimen: two sections located near the ends and the remaining five sections located in the middle of the specimen where the corroded sections were simulated (Fig. 1.8). Each section had seven strain gages distributed uniformly on the web and flanges using one of two profiles, based on the reduced section of the pile (Fig. 1.8).

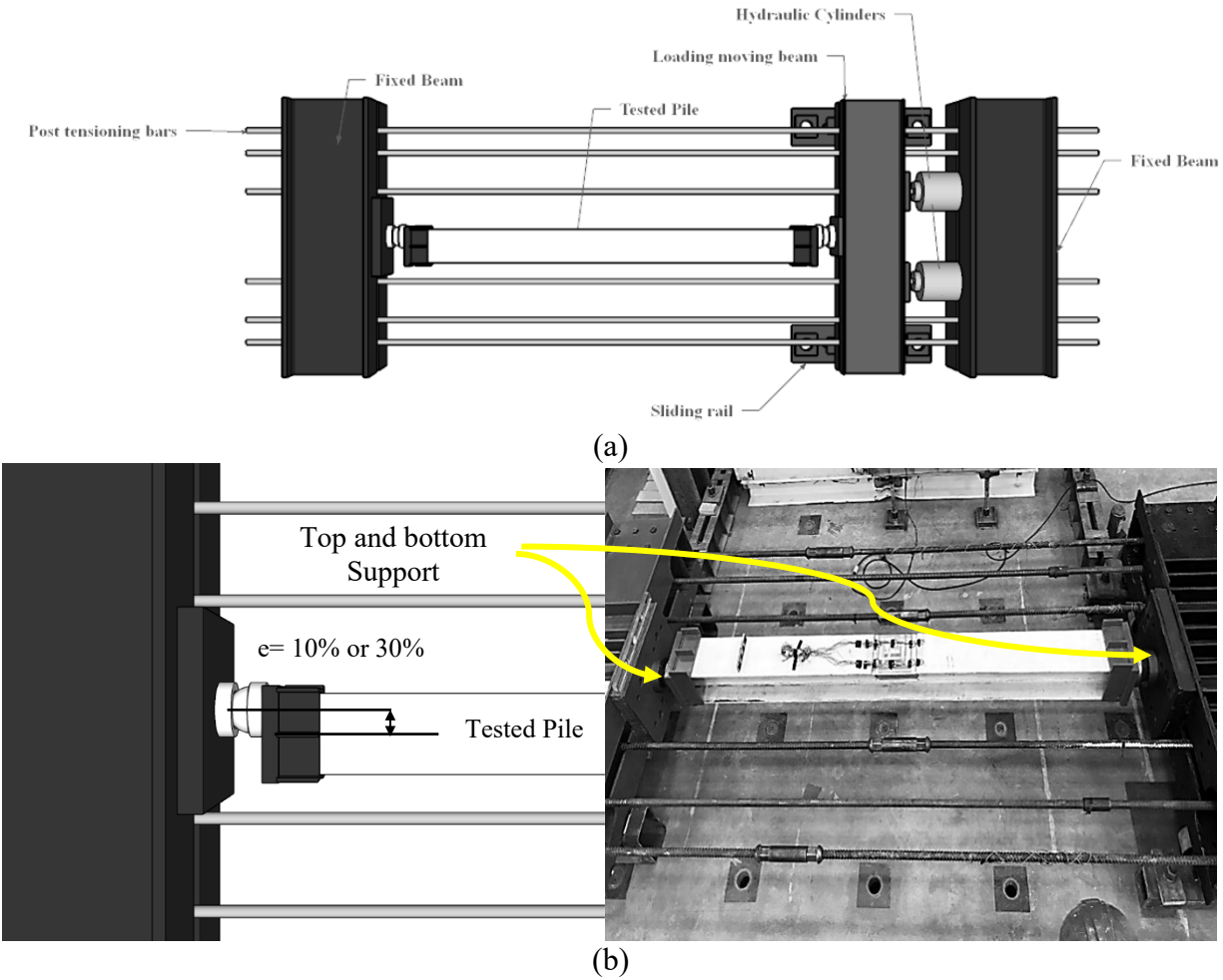


Figure 1.4 Test setup: (a) drawing, and (b) picture.

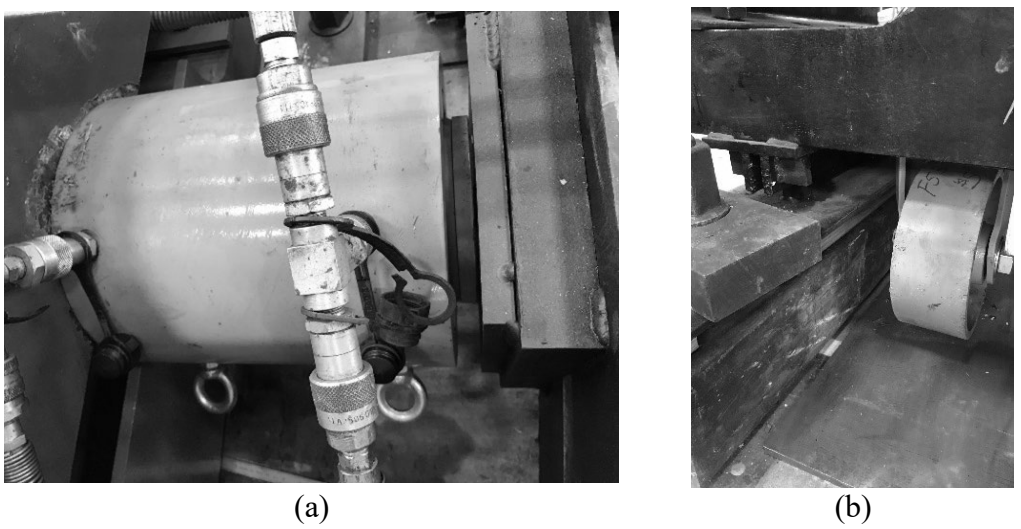
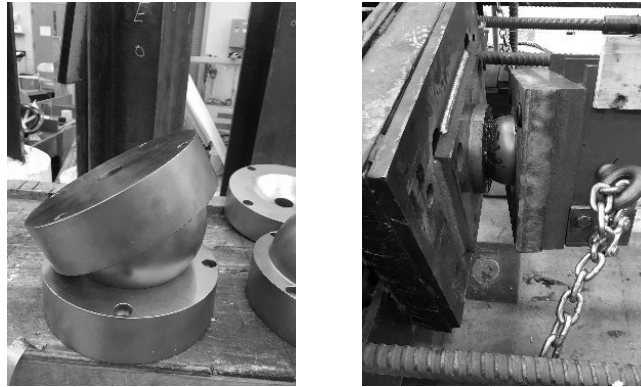


Figure 1.5 Loading instruments: (a) hydraulic jack, and (b) rail track with rolling cylinders.



(a)

(b)

Figure 1.6 Swivel plates (a) maximum rotation, and (b) installed in the setup.

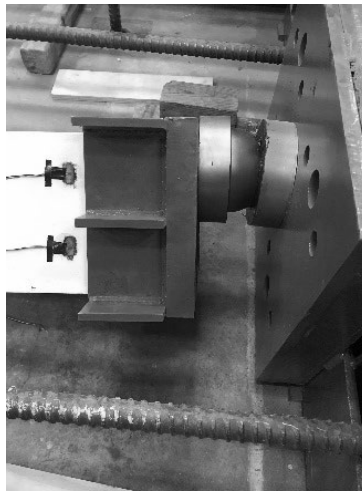
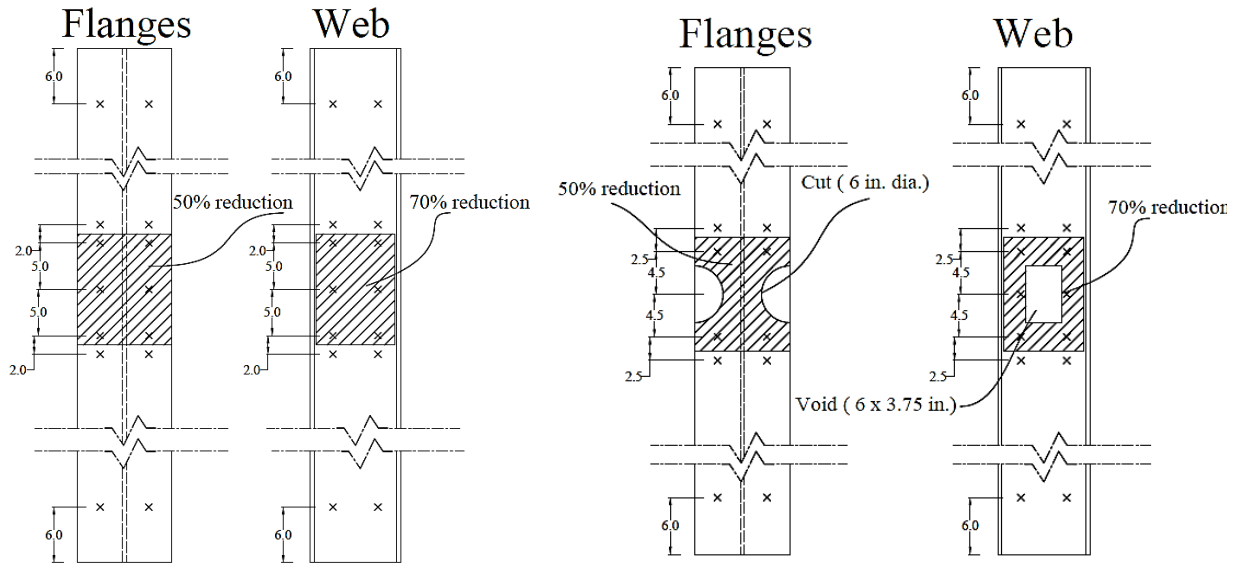


Figure 1.7 Eccentricity of the swivel with the pile.

The Axial shortening of each specimen was measured using three string potentiometers (SPs). Two SPs were connected between the moving beam at one end of the pile and the fixed beam at the other end of the pile. The third SP was connected along the length of each pile. The axial strengths of the piles were calculated using the design procedures of the American Institute of Steel Construction (AISC) [22].



(a) (b)
 Figure 1.8 Distribution of the strain gages on H-piles: (a) Type 1, and (b) Type 2.

Chapter 2 Piles repair design and installation

Three piles were repaired using FRP wrapping filled with concrete (Fig. 1). The required number of FRP layers was determined and applied to each pile. CFRP piles ranging from one to eight had confinement ratios (CR) calculated per equation 2.1 [24].

$$CR = \frac{f_l}{f'_c} = \frac{2t_f E_f \varepsilon_f}{f'_c D_f} \quad (2.1)$$

where f_l is the confining pressure, f'_c is the average unconfined concrete compressive strength, E_f is the CFRP axial modulus of elasticity, t_f is the total thickness of the CFRP jacket, ε_f is the axial ultimate tensile strain of the CFRP, and D_f is the internal diameter of the CFRP jacket.

The required number of shear studs installed on the steel pile was also determined. The shear resistance (P_u (hs)) of the HS was calculated according to provisions for steel headed-stud anchors in composite columns in AASHTO_LRFD [25] (eq. 2.2) to transfer the load, F , from the steel pile to the repair system.

$$P_{u(hs)} = 0.5A_{hs}\sqrt{E_c f'_c} \quad (2.2)$$

For each pile, the required number of HS was passed through holes drilled in the web/flanges. Heavy-duty nuts were installed at the beginning and end of each HS to form a headed stud. The area of a stud, A_{hs} , was calculated using Eq. 2.3 [24].

$$A_{hs} = \frac{\pi}{4} \left(d_a - \frac{0.9743}{n_t} \right)^2 = \frac{\pi}{4} (d_a - 0.0696)^2 \quad (2.3)$$

where n_t = number of threads per inch length of the threaded rod (14 for the used studs), and d_a = diameter of the threaded rod in inches.

2.1 CFRP Jacket

The properties of the CFRP fabrics and Tyfo S epoxy used for applying the CFRP repair jacket were presented in Chapter 3 of this report.

2.1.1 Headed Studs

One-inch diameter all threaded rods having an ultimate strength of 60 ksi were cut to the required lengths and used as headed studs (HSs) (Fig. 2.1). Heavy-duty nuts were added to the ends of each stud to act as stud heads (Fig. 2.2).

2.1.2 Longitudinal Reinforcing Bars

The reinforcing bars have been designed to withstand a bending moment corresponding to an e/t of 5% at the yield strength of the uncorroded H-pile. However, due to the availability and even distributions of the rebar, the bending moment capacity of the rebar corresponded to an e/t of 6.22% at the yield strength of the uncorroded pile. Eight #4 two-leg closed bars with 180 hooks were used (Fig. 2.3). The shape of the bars was selected to ensure there was an adequate development length for #4 bars per ACI 318 (ACI318 2014).



Figure 2.1 All threaded bars and heavy-duty nuts used as HSs.

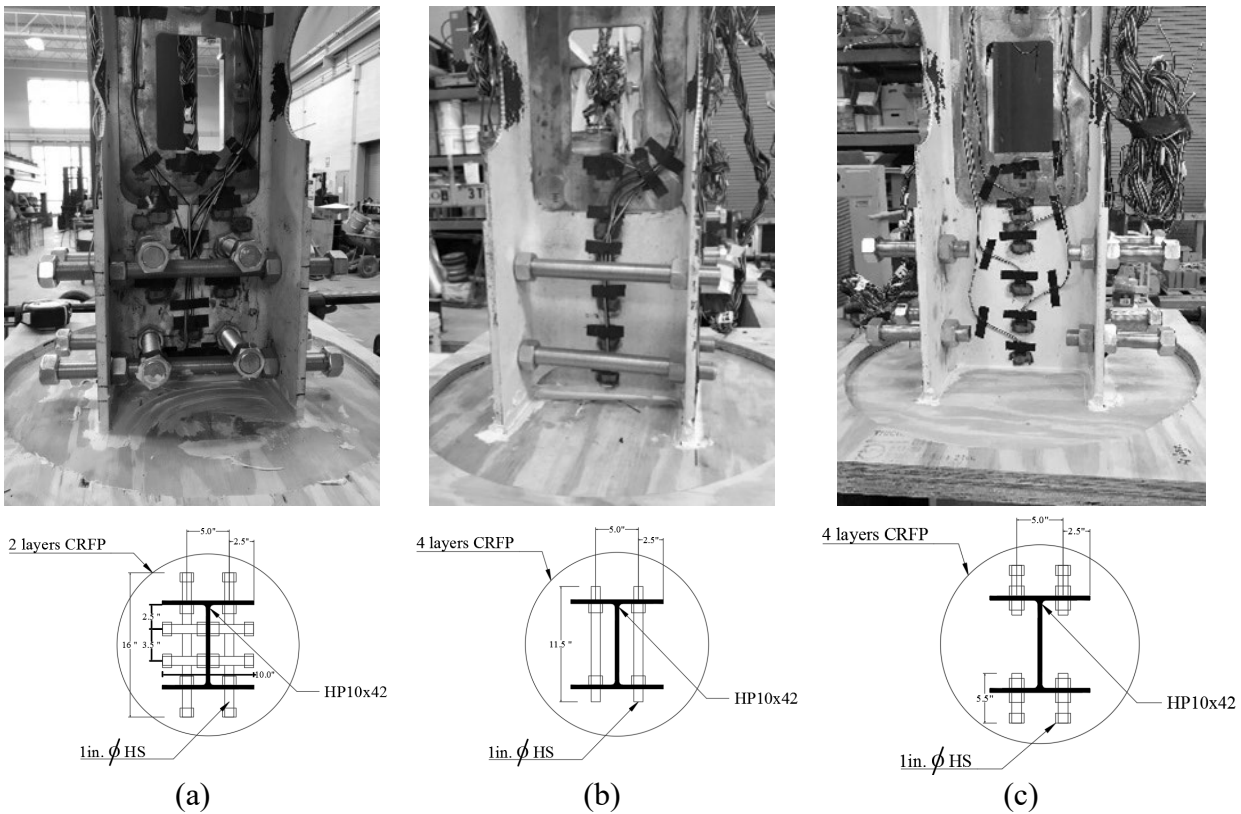


Figure 2.2 Distributions of the HSs in the three H-piles: (a) R-1, (b) R-2, and (c) R-3.

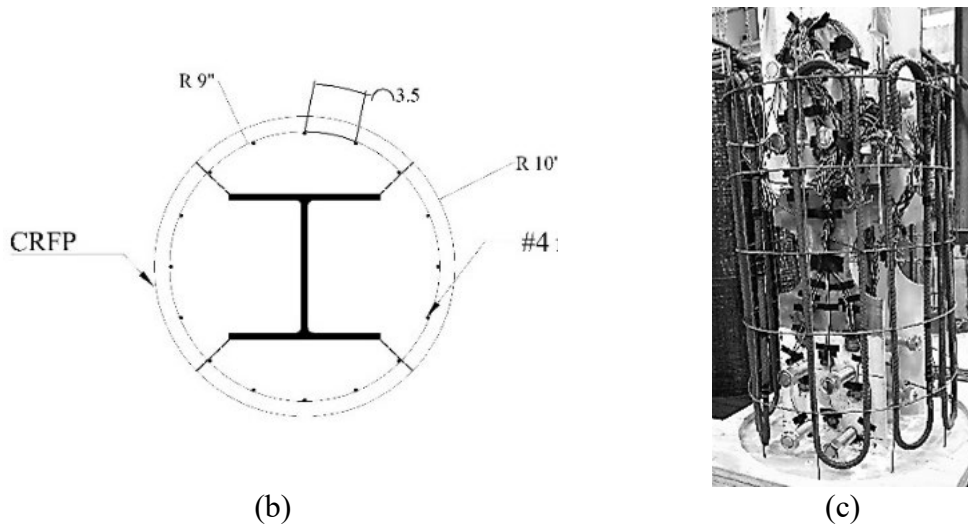


Figure 2.3 Longitudinal reinforcement in the repair region: (a) closed bar profile, (b) distributions of rebars, and (c) reinforcement cage

2.2 Concrete

SCC concrete mix (Table 2.1) was used, to ensure concrete flowability, while filling the CFRP jackets. Three replicate concrete cylinders were tested in compression per ASTM C39 (Standard 2008) and the average concrete compressive on the day of testing of the piles was 7.49 ksi with a standard deviation of 200 psi.

The SCC had a slump flow of 546 mm (21.5 inches) in diameter. Passing ability was tested using J-Ring to determine the flowability of the concrete with a 533 mm (20 inch) diameter (Fig. 2.4). Blocking assessment per ASTM C1611 found the difference between the slump flow and J-ring flow was 12.6 mm (0.5 inch); therefore, there was no visible blocking. An L-box test was also carried out per ASTM C1621.

Table 2.1 Mixture Used for the Concrete

w/c	Cement (lb/yd ³)	Fly Ash (lb/yd ³)	Water (lb/yd ³)	Fine aggregate (lb/yd ³)	Coarse aggregate (lb/yd ³)	HRWR (lb/yd ³)
0.5	350	101	225	848	848	1.9

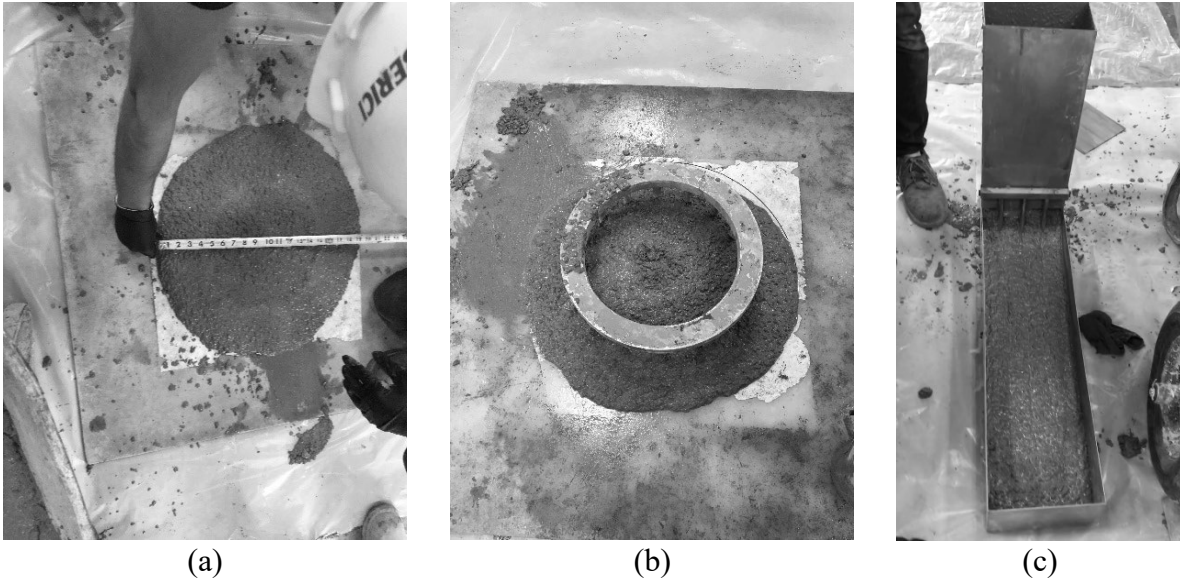


Figure 2.4 ASTM tests: (a) Slump flow, (b) Passing ability using J-ring, and (c) L-box.

2.3 Fabrication and Installation of the Repair System

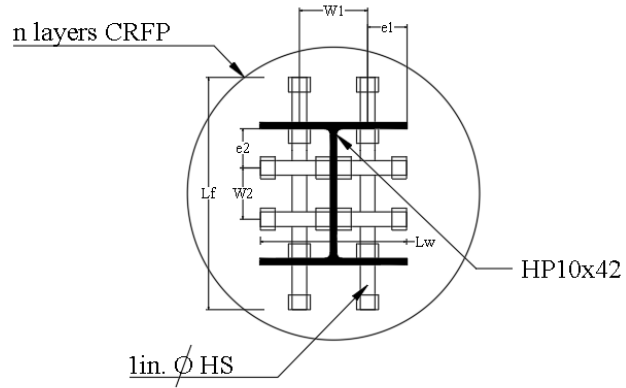
The repair was conducted as follows: (i) preparation of the steel pile, (ii) preparation of the CFRP jackets, (iii) preparation of the steel cage, and (iv) inserting the CFRP repair jacket and filling with SCC.

2.3.1 Preparation of the Steel Pile

After straightening the tested piles to restore their original alignments, the required number of holes for the HSs were drilled in the webs and flanges using a magnetic driller (Fig. 2.5 and Table 2.2).



(a)



(b)

Figure 2.5 (a) Magnetic drill used to drill holes for the HSs, and (b) general distribution for studs

2.3.2 Preparation of the CFRP Jackets

The CFRP was cut to the desired length before a two mm (0.08 inches) thick epoxy layer, per the manufacturer's requirements, was applied to each CFRP jacket. Then, the CFRP jacket was wrapped around a 508 mm (20 inches) diameter Sonotube with an overlap length in the circumferential direction of 203.4 mm (8 inches). The tube diameter was selected to ensure a minimum concrete thickness of 508 mm (2 inches) between the CFRP jacket and the edges of the flanges of the repaired steel H-pile. After one day, the Sonotube was removed from the CFRP jacket.

Table 2.2 Arrangement of HSs in Different Test Specimens

Specimen designation	HSs								CFRP Layers no.
	Flange				Web				
	No.	Lf (in.)	W1 (in.)	e1 (in.)	No.	Lw (in.)	W2 (in.)	e2 (in.)	
R1	2	16	5.0	2.5	2	10	3.5	2.5	2
R2	2	11			N/A	--	--	--	4
R3	4	5.5			N/A	--	--	--	4

2.3.3 Preparation of the Steel Cage

Welded 9-gauge steel wire, 6 x 6 3.75mm (0.148 in.) mesh, was wrapped with a diameter of 19 in. The eight #4 closed reinforcements were uniformly distributed at 88.9 mm (3.5 in.) spacing (Fig. 2.3) and secured in place by attaching them to the wire mesh using steel wires.

2.3.4 Installing the Repair Jacket and Filling with SCC

A 610 x 610 mm (24 x 24 in.) plywood end cap was placed on top of a formwork. The end cap had an H-shaped cut at its center where the prepared steel pile was inserted and aligned in the center of the formwork. The steel and end cap were firmly fixed in their locations using C-clamps that attached the pile to the formwork.

The CFRP jacket was inserted from the top of the corresponding pile and placed atop the end cap. The interface joint between the jacket and end cap was sealed with fast-dry caulk. The steel cage was also inserted from the top of the pile and fixed in place inside the CFRP jacket. SCC filled the CFRP jackets (Fig. 2.6).

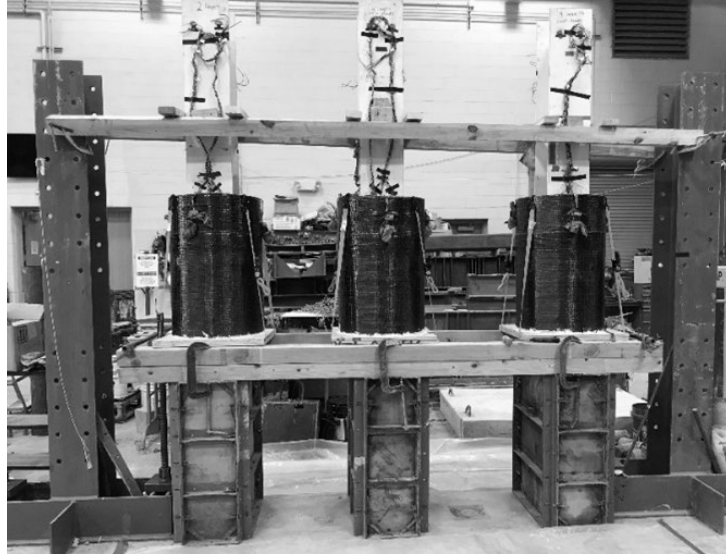


Figure 2.6 Specimens after CFRP Installation

2.3.5 Instrumentation

Ninety-two strain gauges were attached to the web and flanges of each H-pile specimen (Fig. 2.7) before casting the concrete to measure the axial strains.

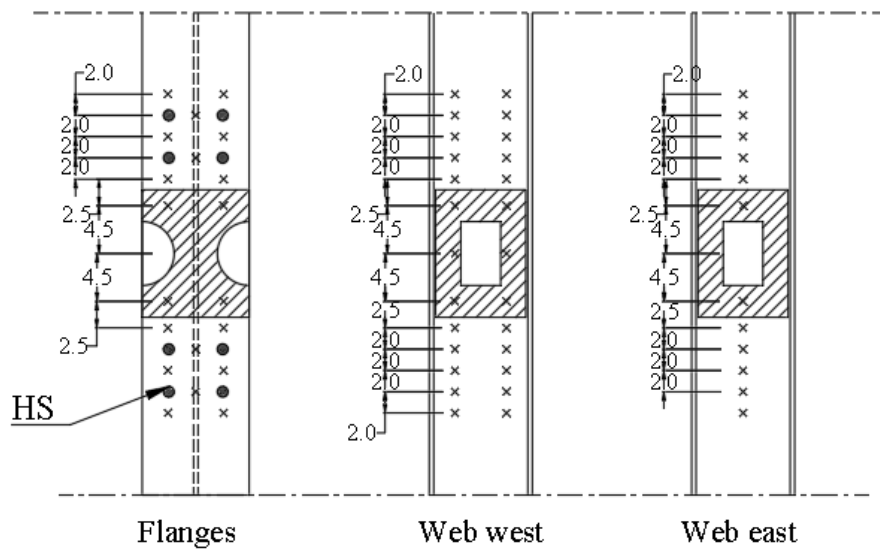


Figure 2.7 Strain gauges distribution on the flanges and web of H-pile

Additional twelve strain gauges were mounted on each CFRP jacket to measure the hoop strains during testing (Fig. 2.8). Twelve strain gauges were attached to the longitudinal rebars to monitor the axial strains. Eight string pots were installed to measure the displacements of each H-pile in both the horizontal and vertical directions (Fig. 2.8).

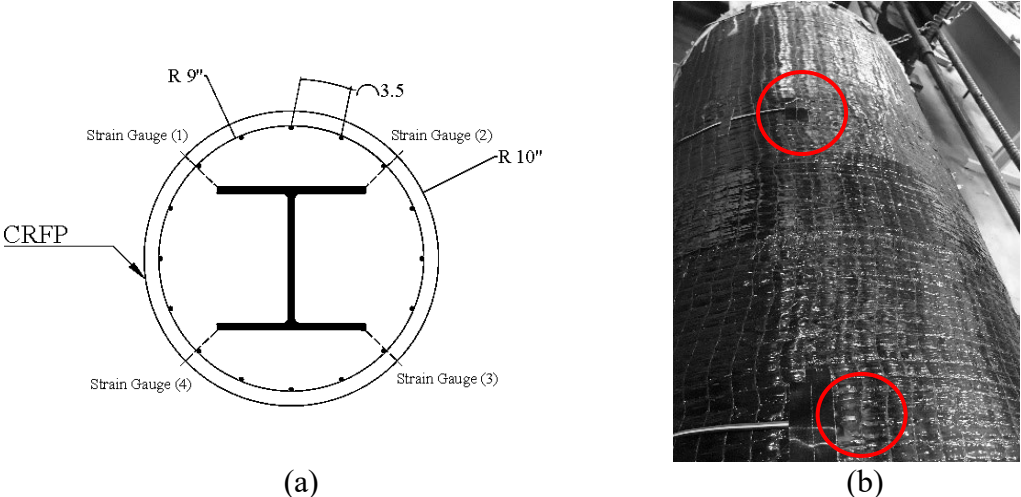


Figure 2.8 Strain gauges distribution on the CFRP cross-section (a) Cross section (b) longitudinal direction

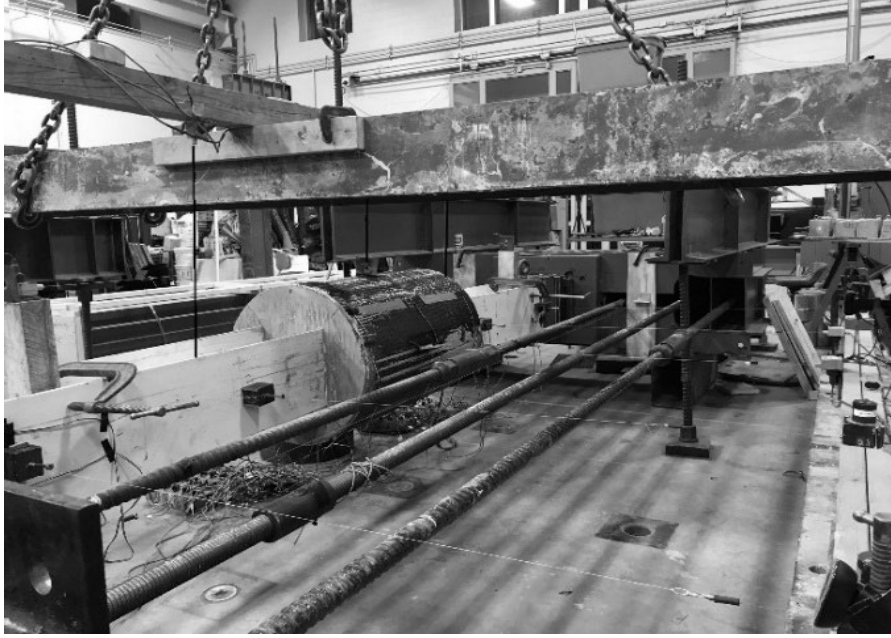


Figure 2.9 String potentiometer vertical and horizontal measurements

Once the CFRP jackets were filled with concrete, they were left to cure at an ambient temperature of $23 \pm 2^\circ \text{C}$ ($73 \pm 3^\circ \text{F}$) inside the laboratory (Fig 2.6). The formwork was removed after three days, and the piles were installed in the test setup described in Chapter 2 of this report. The specimens were axially loaded (Fig. 2.9) and the test results are discussed in the next chapter.

Chapter 3 Piles Testing

The test specimens had pin-pin boundary conditions. Each end of the pile was placed inside a steel shoe, which in turn was connected to a half-sphere that was allowed to rotate on a swivel plate connected to the exterior beam at one end of the pile or the movable beam at the other end of the pile (Fig. 1.4). The required eccentricity was applied by shifting the swivel plate to the required eccentricity. The load was applied monotonically until rupture occurred and the test specimen becomes unstable.

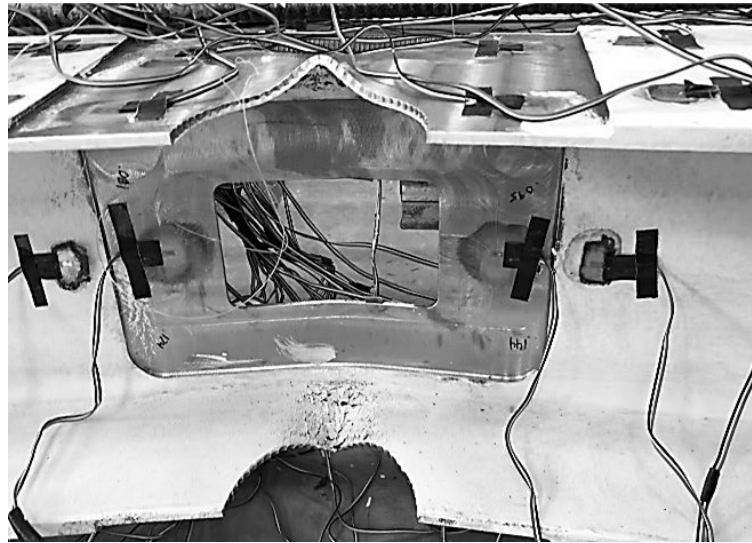
3.1 Results and Discussion

Table 3.1 shows the results for the tested piles. The web of W00-F00 yielded at one end of the pile followed by local buckling of the flanges which gradually dropped the pile strength until it failed at an axial load of 2970 kN (669 kips) (Fig. 3.1). Similarly, W70V-F50C-0% suffered from the flange and web yielding locally at 667 kN (150 kips), which triggered global buckling at the middle section of the pile. Then the load dropped gradually until all strength was lost at the cross-section. (Fig. 3.2).

For the severe corrosion specimens, piles W70V-F50C-10% and W70V-F50C-30% failed at 290 kN (65 kips) and 174 kN (39 kips) with a 57% and 74% drop in capacity, respectively compared to the similar pile with no eccentricity, where the flange and web suffered from local yielding that triggered global buckling at the critical section on the middle at the axial shortening of 5.1 mm (0.2 in.) and 4.8 mm (0.19 in.), respectively. Here the piles sustained a residual capacity of 267 kN (15 kips) and 89 kN (20 kips), which represents 23% and 51% of the peak load at a displacement of 50.8 mm (2 in.) (Fig.3.2).



(a)



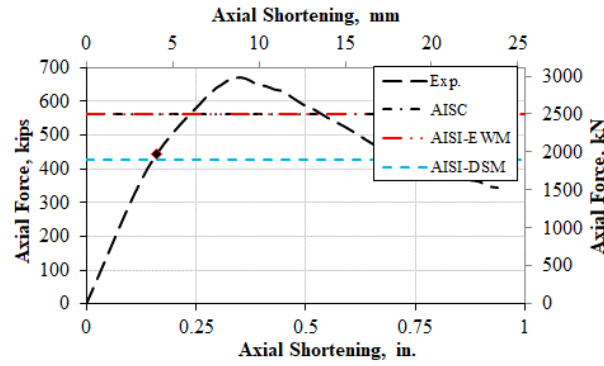
(b)

Figure 3.1 Failure during the experimental W00-F00, and (b) W70V-F50C

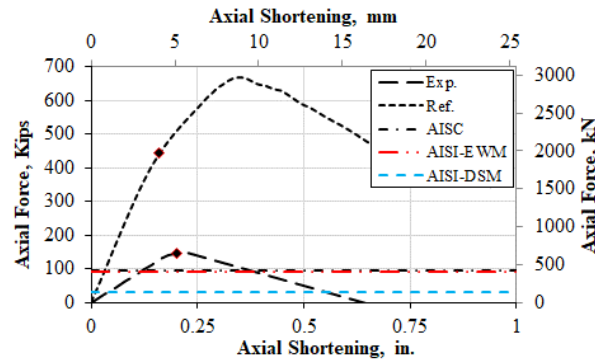
Table 3.1 Results for the Tested Piles

Groups	Pile	Axial Capacity	Axial Shortening	Modes of failure
		Kips	in.	
Reference	W00-F00 [17]	669	0.40	
Severe	W70V-F50C [17]	150	0.25	FLB, WLB
	W70V-F50C-10%	65	0.13	GB
	W70V-F50C-30%	39	0.17	GB

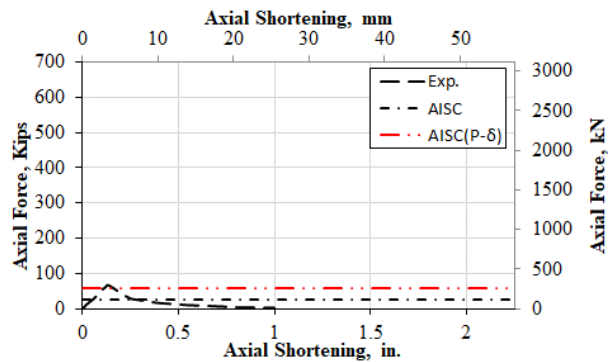
*1 kips=4.45 kN, 1in. = 25.4 mm
 * FLB: Flange Local Buckling, WLB: Web Local Buckling, GB: Global Buckling



(a)



(b)



(c)

Figure 3.2 Axial force vs Axial shortening relation: (a) W00-F00 (Ref.), (b) W70V-F50C, (c) W70V-F50C-10%, (d) W70V-F50C-30%

When comparing the effect of eccentricity on different groups, it was found the severe corrosion specimens were the most sensitive as the load capacity dropped by 57% with a 10% eccentricity compared to an average of 27% for the same specimens with no eccentricity.

Similarly, for the higher eccentricity of 30%, the severe corrosion group was the most sensitive

group with a drop in capacity of 74% compared to an average of 63% for the same specimens with no eccentricity (Fig.3.2).

Figure 3.3 illustrates the axial force versus axial shortening of the repaired piles. As shown in Figure. 3.3 (a), the peak load of specimen R1 was 2228 kN (490.3 kips) with a capacity increase of 272% from the original pile W70V-F50C.

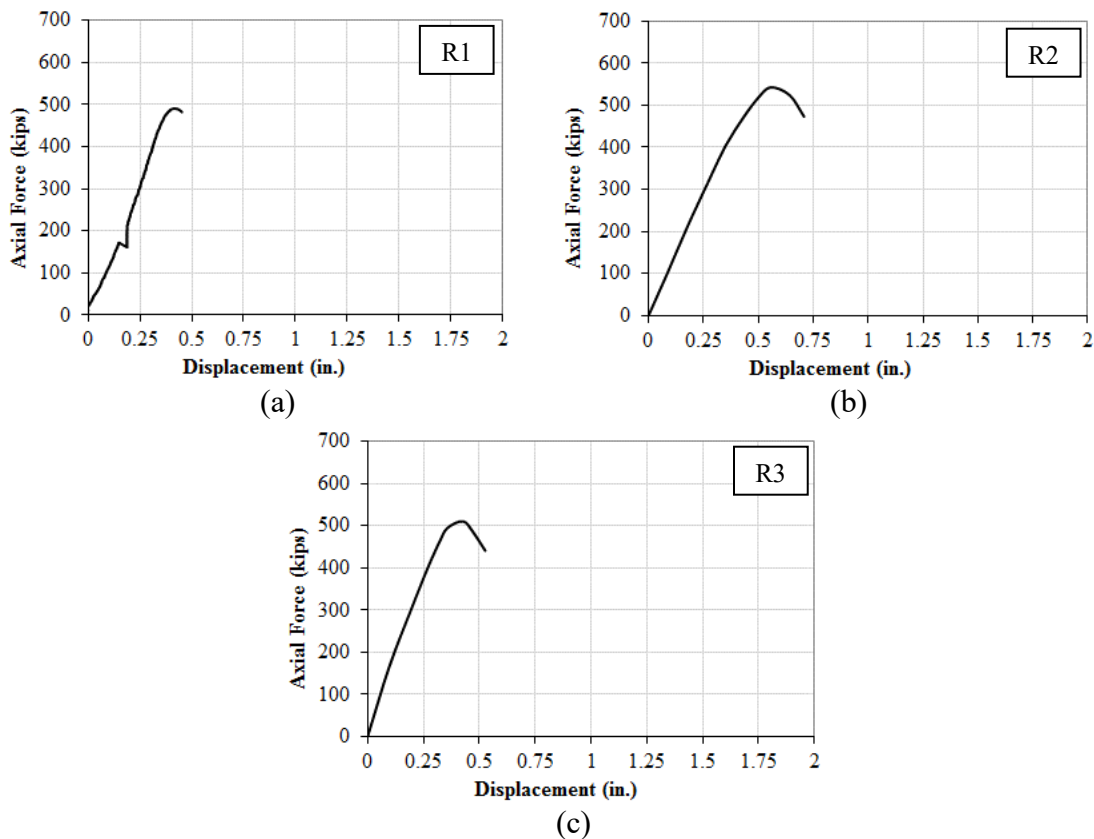


Figure 3.3 Experimental axial load vs. displacement curves (a) R1, (b) R2, and (c) R3

The peak load was accompanied by yielding stress at the section of the steel pile just outside the concrete jacket. For the repaired R2 specimen, the peak load was 2466 kN (542.5 kips) where the pile section locally failed followed by global buckling afterward. For the

repaired R3 specimen, the peak load was 2,318 kN (510 kips) and it failed due to local buckling accompanied by global buckling in the pile (Fig. 3.3).

Chapter 4 Finite element modeling of the repaired piles

4.1 FE Modeling

The finite element modeling was performed using LS-DYNA software. The material properties were determined from tensile coupon tests, and the initial local and overall imperfections were measured from the test specimens before loading. The geometric imperfections were included by using a linear perturbation analysis to establish the probable buckling modes of the column for nonlinear analysis. Residual stresses were not considered since the measurements obtained from Young and Rasmussen (1995, 1998) [26-28] indicated they were negligible.

4.1.1 Model Geometry

The geometric properties and material properties of the repaired steel pile is illustrated in Section 4.1. Figure 4.1 shows the general 3D view of the FE modeled retrofitted piles. A sensitivity analysis was conducted to determine the different element sizes. The element type and size were determined according to a sensitivity study, which indicated that the chosen type and size provided best predictions for the strengths and deformations of the piles. Each FE model had approximately 41,862 elements and 35,857 nodes. Figure 4.2 shows the final finite element model of the different parts of the simulated retrofit steel H-pile.

4.1.2 Material Models

4.1.2.1 Concrete

Release III of the Karagozian and Case (K&C) was used to model the concrete material. The model was developed based on the theory of plasticity and had three shear failure surfaces: (1) yield, (2) maximum, and (3) residual shear. Several investigators used this material model to predict the performance of concrete structures under lateral cyclic loads as implemented by

Abdelkariem et al. (2017) [29]. An automatic option was used during this research to generate all the model parameters, i.e., given the uniaxial unconfined compressive strength f'_c ; the model can create all the constants required for the finite element analysis. The concrete encasement was modeled using constant-stress solid elements, which uses single-point integration and reduces the computational time over the full integration element with accuracy.

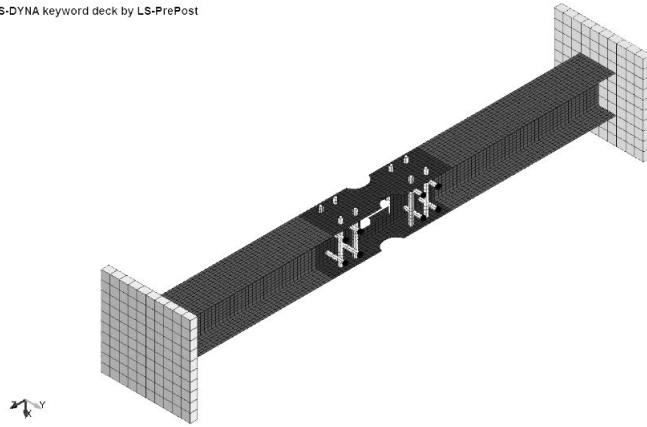
4.1.2.2 CFRP tube

The outer CFRP jacket was simulated using Belytshenko-Tsay four-node shell elements with six degrees of freedom per node. An orthotropic elastic material denoted as 002-orthotropic_elastic was used to simulate the FRP tube. This material was defined by the elastic modulus, shear modulus, and Poisson's ratio in the three principal axes. A failure criterion for the GFRP elements was implemented in LS_DYNA by defining the ultimate strain using *MAT_ADD_EROSION keyword. The elastic moduli of the CFRP tube was 16,200 ksi, the axial elastic moduli and axial ultimate stress of the CFRP jacket was 140 ksi, the rupture strain was 0.85%, and the major Poisson's ratio was 0.4.

4.1.2.3 Headed Stud Connectors

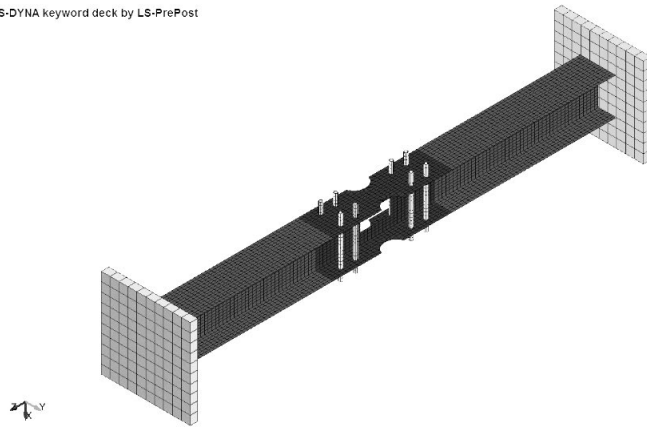
Material model 003-plastic_kinematic was used to model the headed studs in LS-DYNA. This material model considers steel as an elastoplastic material, which can be defined using: (1) the elastic modulus, E; (2) the yield stress; and (3) Poisson's ratio. It has the option of including strain-hardening effects using a linear relationship for plastic behavior. The effective diameter was calculated by considering the effect of threads in reducing the cross-sectional area. Table 6.3 summarizes the properties of the simulated headed studs.

LS-DYNA keyword deck by LS-PrePost



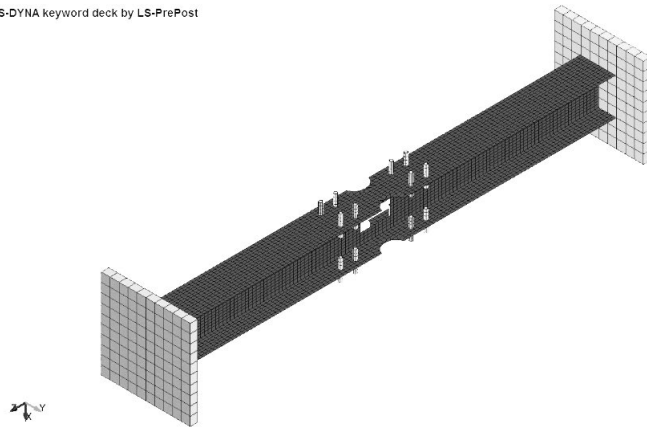
(a)

LS-DYNA keyword deck by LS-PrePost



(b)

LS-DYNA keyword deck by LS-PrePost



(c)

Figure 4.1 FE of the repaired piles and HSs layout of (a) R1, (b) R2, and (c) R3.

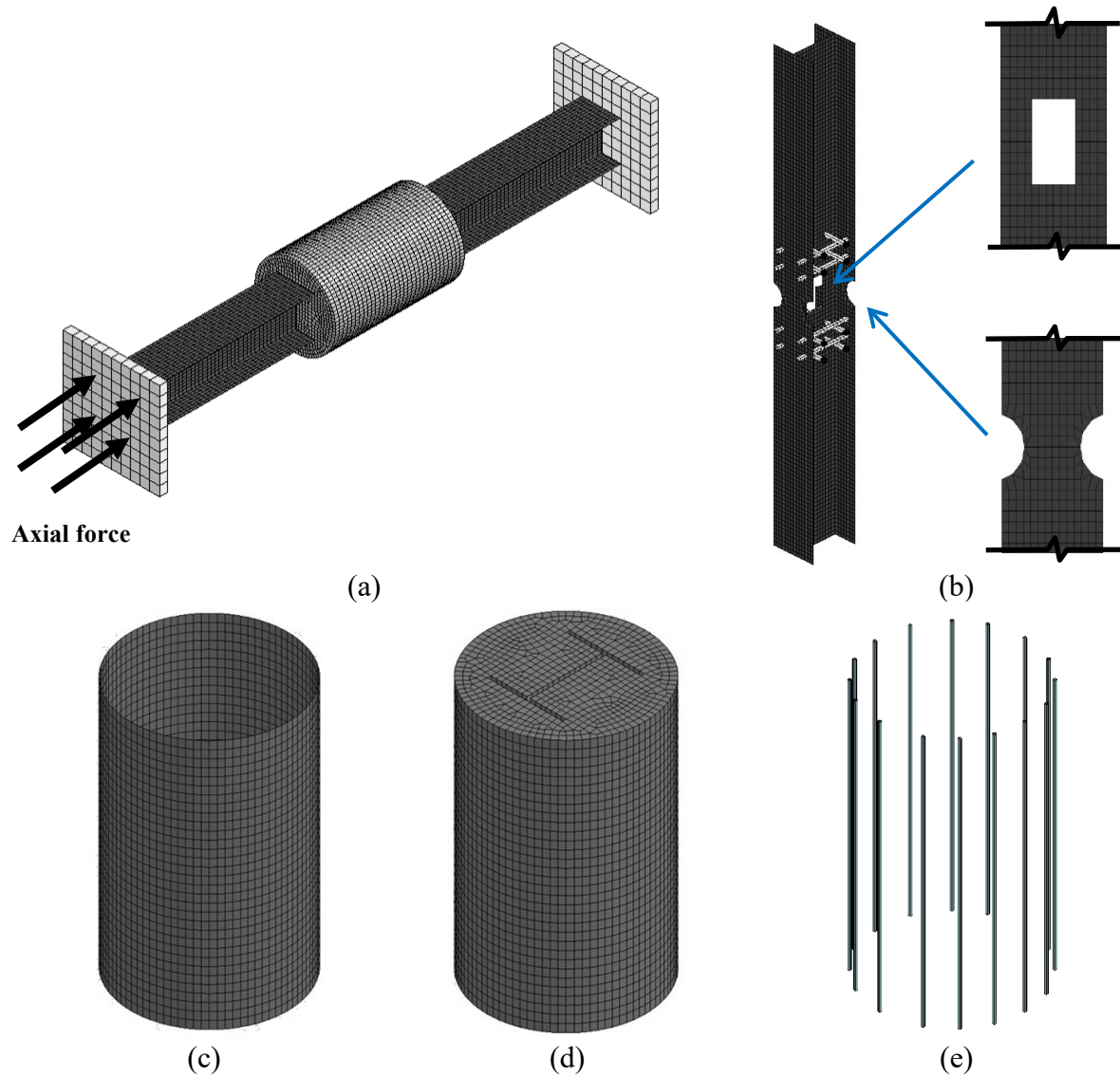


Figure 4.2 FE modeling: (a) 3D view of the repaired steel pile, (b) steel H-pile, (c) CFRP tube, (d) concrete filling, and (e) steel rebar.

4.1.2.4 Steel Rebars

The steel rebars are modeled using truss-rebar elements. The steel rebars were included explicitly using the constrains method. The rebars were embedded into the concrete encasement using constrains-lagrange-in-solids (CLIS) input. The required inputs were the part IDs of the

rebars (as the slave) coupled to the concrete (as the master). Table 4.1 summarizes the properties of the simulated headed studs.

Table 4.1 Mechanical Properties of the Steel Rebar Elements

Diameter (in)	Tensile modulus (ksi)	Yield strength (ksi)	Poisson's ratio
0.25	29,000	75	0.3

4.1.3 Boundary Conditions and Loading

Boundary conditions were modeled to represent the test set-up at the supports. At the fixed end of the pile, translation was restrained in three perpendicular directions. At the jacking end, translation was restrained in the global X and Y directions, but the pile was free to translate in the axial, global Z, direction. The piles were loaded by imposing an axial displacement at one end to simulate the action of the hydraulic jack in the experimental program.

Surface-to-surface contact elements were used to simulate the interface between the CFRP jacket and the concrete encasement. In this approach, the master and slave surfaces are generated internally within LS-DYNA from the parts ID's given for each surface. Contact elements surface-to-surface were also used to simulate the interface between the CFRP jacket and the concrete encasement and between the concrete encasement and the steel pile. Node-to-surface contact elements were used between the loading plates and the steel pile ends. The coefficient of friction for all the contact elements was taken as 0.6. The hourglass stiffness-based control type and coefficient used during this study were 5 and 0.03, respectively.

Initial perturbations were produced using the "perturbation" with "shell-thickness" keyword option in LS-DYNA software where the shell thickness was perturbed for the specific shell set on the simulated steel pile shell surface.

4.1.4 Model Results

4.1.4.1 Axial Load-Displacement

Figure 4.3 shows the axial load vs displacement curves of the the FE results compared to the obtained experimental results. In general, the FE model shows a good correlation with the test results for ultimate loads, stiffness, and onset of non-linearity.

The repaired piles with 70% void in the web and 50% cut in the flange thickness demonstrated a localized failure mode in the experimental test. The FE model was able to predict the axial-load displacement response and pre-peak behavior for the piles accurately. Comparison of the measured and predicted responses and peak loads for these piles suggests that failure was imminent. For the piles with 70% reduction in the thickness of the flanges, the onset of non-linearity of the repaired piles was predicted accurately. However, the initial stiffness was accurately predicted for the retrofitted steel pile R1, while it was 10% and 6% higher than the measured values for piles R2 and R3, respectively.

This occurred as the steel piles underwent large plastic deformation during straightening the piles prior to the repair. Hence, large residual stresses were generated, and it was difficult to simulate them accurately in the FE.

4.1.4.2 Failure Modes

The predicted failure modes of the simulated piles R1 and R3 were flange local buckling outside of the repaired region followed by global lateral deformation (Figs. 4.4). As shown in Figure 6.14, by comparing the deformed shape of the tested piles and the corresponding deformed shape obtained from the FE models, the model accurately predicted the failure mode and deformation pattern of these two tested piles (Fig. 4.14). Figure 6.14 (a and b) shows the global deformation of the repaired pile after 12.7 mm (0.5 in.) axial displacement.

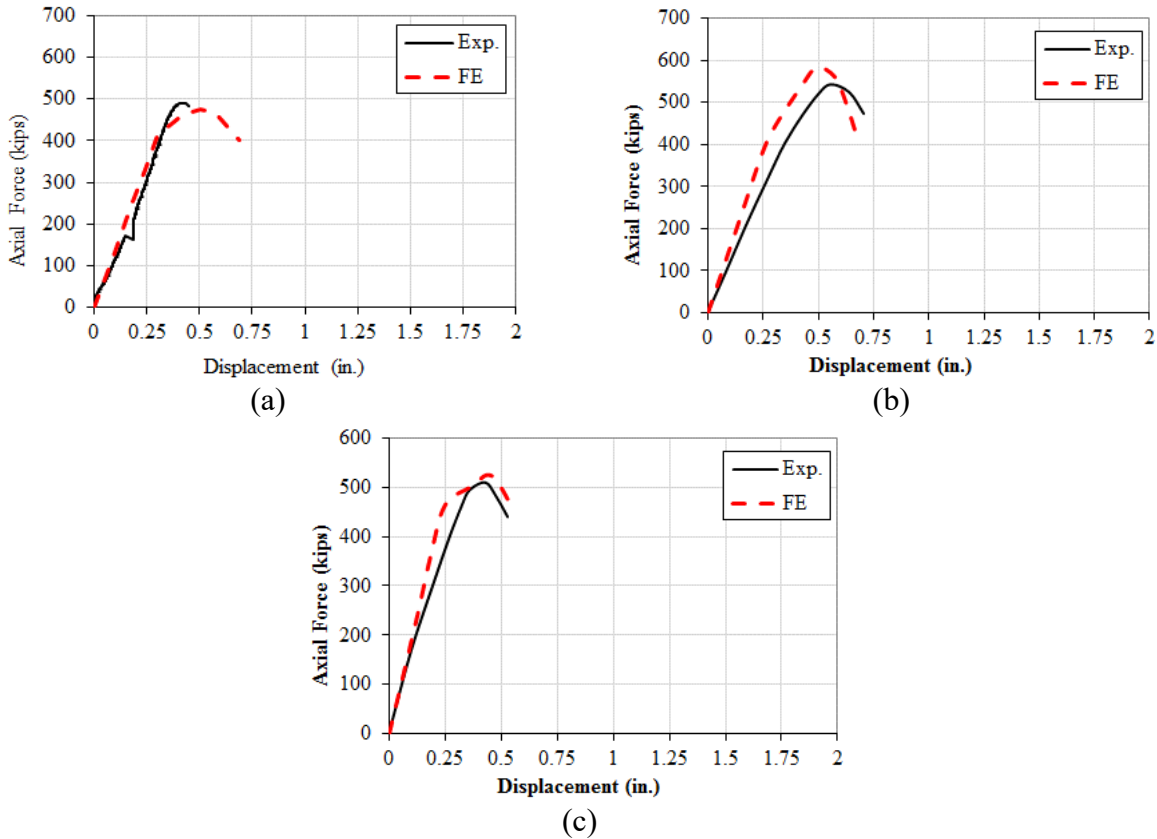
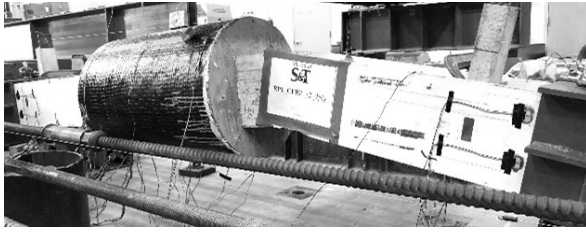
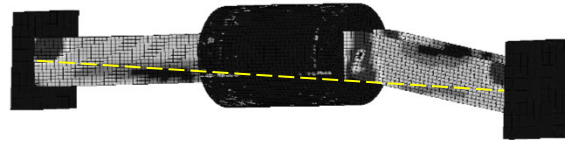


Figure 4.3 Axial load vs. displacement curves (a) R1, (b) R2, and (c) R3.

Figure 4.4 (c and d) shows a closer view of the steel pile-damaged region, where the steel pile section yielded and then buckled at a distance of 940 mm (37 in.) from the loading plate. Figure 4.4 (e) reveals some stress concentration appeared in the simulated concrete encasement, observed as minor cracks in the experimental test (Fig. 4.5). Figure 4.4 (f) indicates stress concentrations in the middle of the CFRP jacket at the ultimate loading stage.



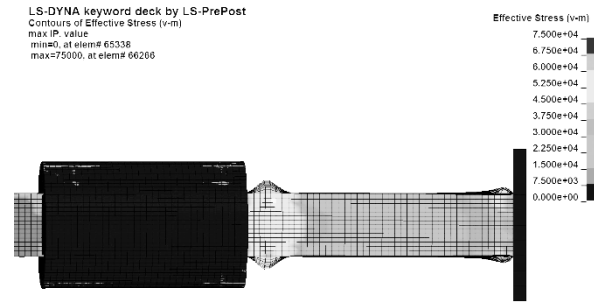
(a)



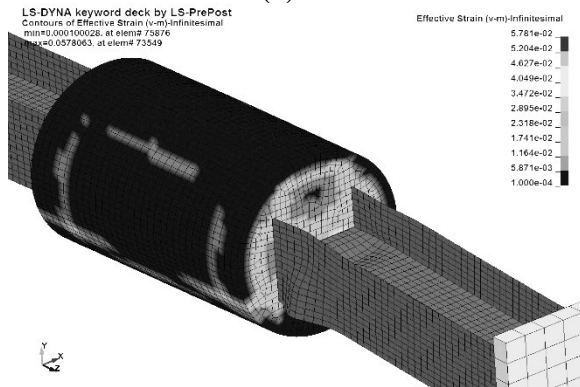
(b)



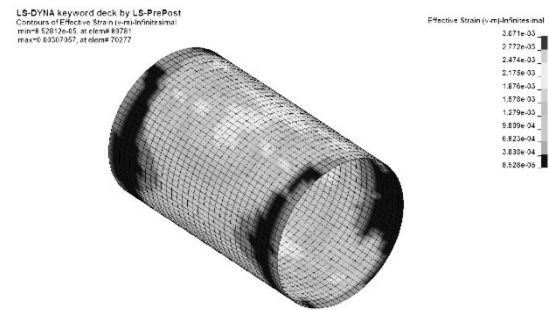
(c)



(d)



(e)



(f)

Figure 4.4 Failure modes of the simulated repaired pile R1 (a) exp., (b) FE whole system, (c) Exp. steel pile localized buckling, (d) FE steel pile localized buckling, and (e) concrete encasement stress concentration

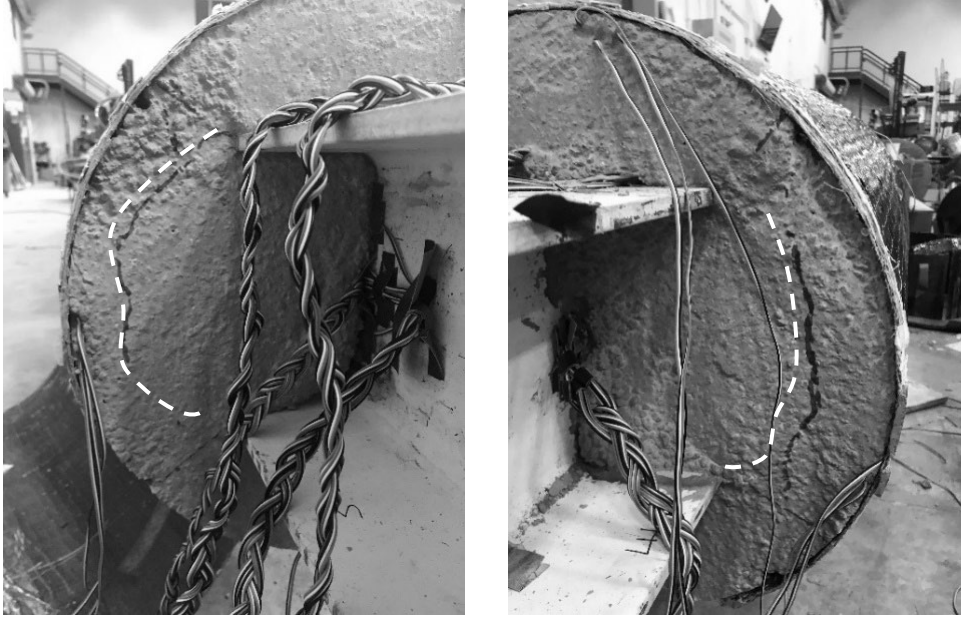


Figure 4.5 Stress concentration at the tips of flanges on the concrete encasement.

This is due to the thinnest CFRP jacket used in R1 (2-ply) method compared to the other methods (with 4-ply) was less stiff in the hoop direction. Moreover, the large concrete encasement expansion occurred in that region. No rupture was found in the simulated CFRP jacket, matching the experimental test observations. Figure 4.6 indicates stress concentrations at the tips of the flanges in the CFRP jacket at the ultimate loading stage for pile R2. This pile demonstrated rupture of the CFRP jacket, which occurred along the tips of the bottom flange of the simulated pile.

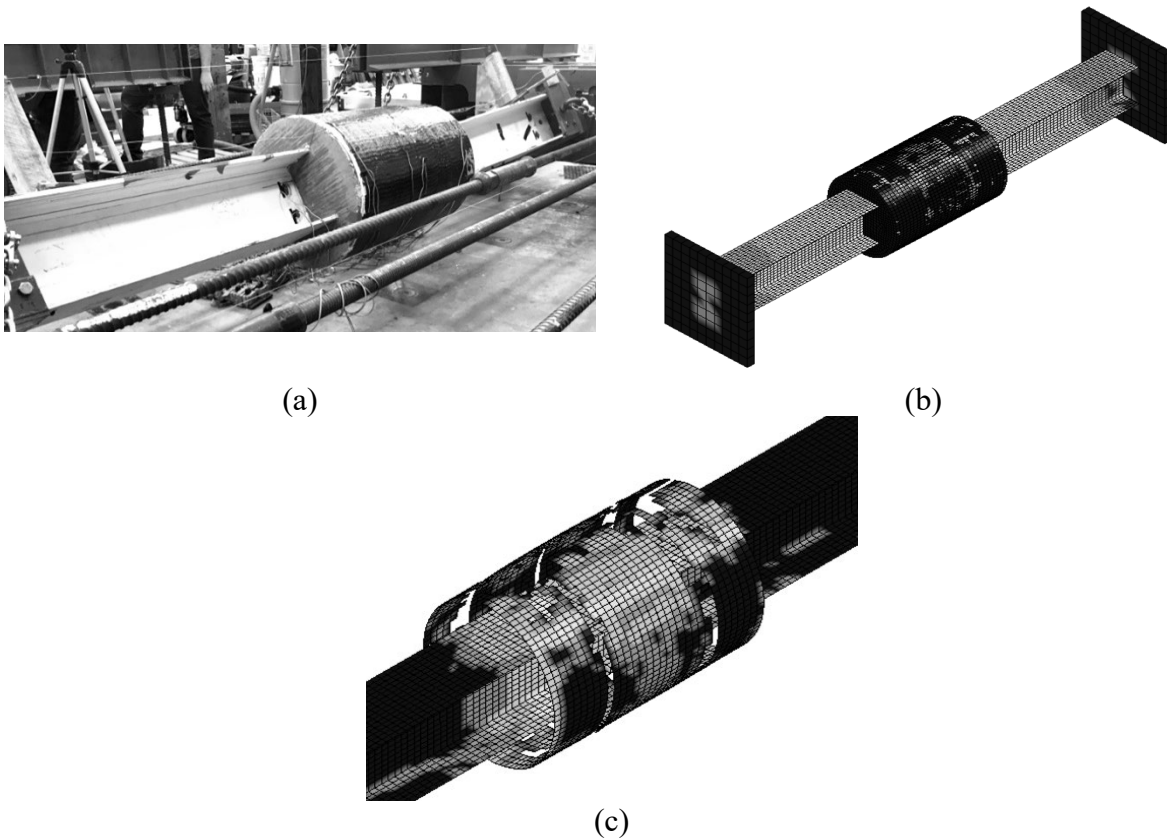


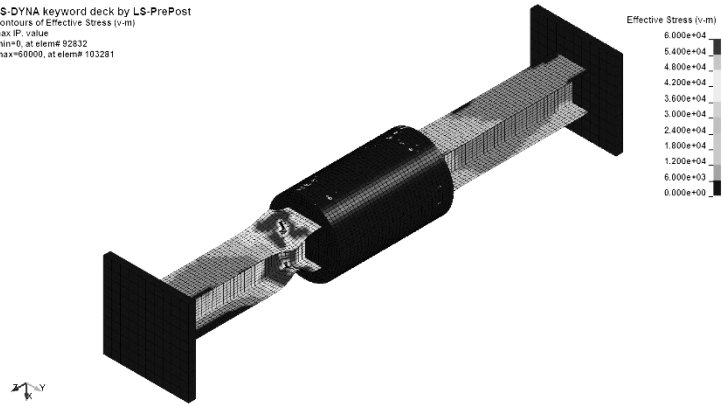
Figure 4.6 Failure modes of the simulated repaired pile R2 (a) exp., (b and c) FE.

The FE model shows a large concrete encasement expansion at the flange sides towards the CFRP jackets leading to high hoop stress on the latter followed by rupture. However, this was not observed with the tested pile using R2 where no CFRP rupture was noticed (Fig. 4.6).



(a)

LS-DYNA keyword deck by LS-PrePost
 Contours of Effective Stress (v-m)
 max IP value
 min=0, at elem# 82832
 max=66009, at elem# 103281

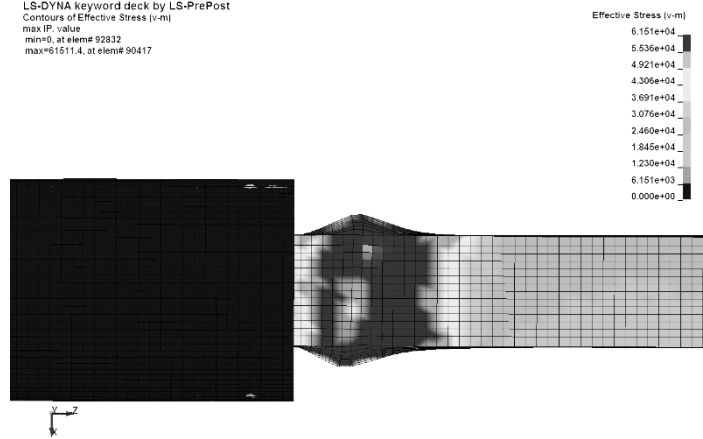


(b)



(c)

LS-DYNA keyword deck by LS-PrePost
 Contours of Effective Stress (v-m)
 max IP value
 min=0, at elem# 92832
 max=61511.4, at elem# 90417



(d)

Figure 4.7 Failure modes of the simulated repaired pile R3 (a and c) exp., (b and d) FE.

Chapter 5 Summary And Conclusions

Four full-scale H-piles were tested under eccentric axial loads. The piles contain a reference pile and three have a corroded section to simulate severe corrosion. The piles were tested under axial loads having eccentric loadings of 10% and 30%. The corrosion was simulated using a mechanical reduction in the thickness and cuts in the flanges and/or webs of the piles. The axial strengths of the piles were calculated using a design procedure by the AISC. The following conclusions can be drawn from the current study:

- Eccentricity has a significant effect on corroded H-piles, especially in severe corrosion cases. For example, in the case of reduction in the flange and web of 50% and 70% combined with cuts in the flange of 152 mm (6in.) diameter and 101 x 101 mm (4 x 4 in.) voids in the web, the capacity dropped by 57% when 10% eccentricity was introduced and 76% with 30% eccentricity compared to the concentric pile.
- Flange reduction has the most significant effect on the axial capacity of corroded H-piles subjected to eccentric loading. For example, when the thickness of the web was reduced by 90% with 10% eccentricity, the load dropped by 44% from the concentrically loaded pile; while when there was 90% reduction with 30% eccentricity, the load dropped by 75%.
- The repaired piles with eight 25.4 mm (1 in.) diameter headed studs anchored to the web of the H-pile and eight plies of CFRP reached a maximum axial capacity of 2,403 kN (540.3 kips), representing 82% of the pile yielding load. Similar strength was achieved with three plies of CFRP and eight-headed studs anchored to the flanges of the H-pile.
- The FEMs for the retrofitted piles accurately predicted the axial load vs displacement curves. The difference between the ultimate capacity obtained using the FEMs and those obtained during the experimental work was less than 10%. Moreover, the FEMs accurately

predicted the failure modes and deformation patterns of the experimentally tested piles R1 and R3, which failed due to localized buckling that occurred outside of the repair region with no CFRP rupture. For the retrofitted pile R2, the FEM predicted CFRP rupture while the experimental work displayed concrete cracking inside the CFRP jacket. However, this crack did not trigger CFRP rupture, and the pile failed due to localized buckling that occurred outside of the repair region.

References

1. Hannigan, P.J., et al., *Design and construction of driven pile foundations–Volume I*. 2016, National Highway Institute (US).
2. Romanoff, M., *Corrosion of steel pilings in soils*. Vol. 58. 1962: US Government Printing Office.
3. Kayser, J.R. and A.S. Nowak, *Capacity loss due to corrosion in steel-girder bridges*. *Journal of Structural Engineering*, 1989. 115(6): p. 1525-1537.
4. Fisher, J.W., B.T. Yen, and D. Wang, *Fatigue strength of riveted bridge members*. *Journal of Structural Engineering*, 1990. 116(11): p. 2968-2981.
5. Bruneau, M. and S.M. Zahrai, *Effect of severe corrosion on cyclic ductility of steel*. *Journal of Structural Engineering*, 1997. 123(11): p. 1478-1486.
6. Bruneau, M., C.-M. Uang, and A. Whittaker, *Ductile design of steel structures*. Vol. 389. 1998: McGraw-Hill New York.
7. Hays, G.F. and P.D. General, *World corrosion organization*. Corrodia. NACE International, Houston, 2010.
8. FHWA, *National Bridge Inventory*. U.S. Department of Transportation, Federal Highway Administration, 2015.
9. Paik, J., J. Lee, and M. Ko, *Ultimate compressive strength of plate elements with pit corrosion wastage*. *Proceedings of the Institution of Mechanical Engineers, Part M: Journal of Engineering for the Maritime Environment*, 2003. 217(4): p. 185-200.
10. Liu, X., A. Nanni, and P.F. Silva, *Rehabilitation of compression steel members using FRP pipes filled with non-expansive and expansive light-weight concrete*. *Advances in Structural Engineering*, 2005. 8(2): p. 129-142.
11. Ok, D., Y. Pu, and A. Incecik, *Computation of ultimate strength of locally corroded unstiffened plates under uniaxial compression*. *Marine Structures*, 2007. 20(1-2): p. 100-114.
12. Beaulieu, L.-V., F. Legeron, and S. Langlois, *Compression strength of corroded steel angle members*. *Journal of Constructional Steel Research*, 2010. 66(11): p. 1366-1373.
13. Saad-Eldeen, S., Y. Garbatov, and C.G. Soares, *Experimental assessment of the ultimate strength of a box girder subjected to severe corrosion*. *Marine Structures*, 2011. 24(4): p. 338-357.

14. Jiang, X. and C.G. Soares, *Ultimate capacity of rectangular plates with partial depth pits under uniaxial loads*. Marine Structures, 2012. 26(1): p. 27-41.
15. Jiang, X. and C.G. Soares, *A closed form formula to predict the ultimate capacity of pitted mild steel plate under biaxial compression*. Thin-walled structures, 2012. 59: p. 27-34.
16. Karagah, H., et al., *Experimental investigation of short steel columns with localized corrosion*. Thin-Walled Structures, 2015. 87: p. 191-199.
17. Abdulazeez, Mohanad M., Amro Ramadan, Binod Sherstha, Ahmed Ghenni, Eslam Gomaa, Yasser Darwish, and Mohamed ElGawady. *Behavior and Repair of Corroded Steel H-Piles Phase I (Axial Behavior)*. No. 25-1121-0005-133-1. Mid-America Transportation Center, 2019.
18. Ramadan, A., *Assessment and retrofitting of corroded steel H-piles in Civil Engineering*. 2020, Missouri University of Science and Technology.
19. Sarveswaran, V., J. Smith, and D. Blockley, *Reliability of corrosion-damaged steel structures using interval probability theory*. Structural Safety, 1998. 20(3): p. 237-255.
20. AISC, *American Institute of Steel Construction, 13th Ed*. Steel construction manual. 13th edition, 2005.
21. Karagah, H. and M. Dawood. *Axial capacity of partially corroded steel bridge piles*. in *Proceeding of the annual stability conference*. St. Louis, Missouri. 2013.
22. *ASTM E8/E8M-16a (2016) Standard Test Methods for Tension Testing of Metallic Materials*. ASTM International, West Conshohocken.
23. AISC, *American Institute of Steel Construction, 15th Ed*. Steel construction manual. 15th edition, 2017.
24. ACI PRC-440.1-15, *Guide for the Design and Construction of Structural Concrete Reinforced with Fiber-Reinforced Polymer Bars*, Farmington Hills, MI, USA, 2015.
25. AASHTO, LRFD. "American Association of State Highway and Transportation Officials LRFD Bridge Design Specifications." *Washington DC* (2012).
26. Young, B., & Rasmussen, K. J. R. (1995a). *Compression Tests of Fixed-Ended and Pin Ended Cold-Formed Lipped Channels*. Research Report-University of Sydney School of Civil and Mining Engineering R.
27. Young, B., & Rasmussen, K. J. R. (1995b). *Compression tests of fixed-ended and pin-ended cold-formed plain channels*. Research Report-University of Sydney School of Civil and Mining Engineering R.

28. Young, B., & Rasmussen, K. J. (1999). Behaviour of cold-formed singly symmetric columns. *Thin-walled structures*, 33(2), 83-102
29. Abdelkarim, Omar I., Mohamed A. ElGawady, Ahmed Ghani, Sujith Anumolu, and Mohanad Abdulazeez. "Seismic performance of innovative hollow-core FRP-concrete-steel bridge columns." *Journal of Bridge Engineering* 22, no. 2 (2017): 04016120.